Morgan, AN, Perley, DA, Cenko, SB, Bloom, JS, Cucchiara, A, Richards, JW, Filippenko, AV, Haislip, JB, LaCluyze, A, Corsi, A, Melandri, A, Cobb, BE, Gomboc, A, Horesh, A, James, B, Li, W, Mundell, CG, Reichart, DE and Steele, IA

Evidence for dust destruction from the early-time colour change of GRB 120119A

Monthly Notices
of the
ROYAL ASTRONOMICAL SOCIETY
MNRAS (2014) doi:10.1093/mnras/stu344

Evidence for dust destruction from the early-time colour change of GRB 120119A

Adam N. Morgan,[1⋆] Daniel A. Perley,[2] S. Bradley Cenko,[1] Joshua S. Bloom,[1] Antonino Cucchiara,[3] Joseph W. Richards,[1,4] Alexei V. Filippenko,[1] Joshua B. Haislip,[5] Aaron LaCluyze,[5] Alessandra Corsi,[6] Andrea Melandri,[7,8] Bethany E. Cobb,[6] Andreja Gomboc,[9,10] Assaf Horesh,[2] Berian James,[1,11] Weidong Li,[1†] Carole G. Mundell,[8] Daniel E. Reichart[5] and Iain Steele[8]

[1]*Department of Astronomy, University of California, Berkeley, CA 94720-3411, USA*
[2]*Department of Astronomy, California Institute of Technology, Pasadena, CA 91125, USA*
[3]*Department of Astronomy and Astrophysics, UCO/Lick Observatory, University of California, Santa Cruz, CA 95064, USA*
[4]*Department of Statistics, University of California, Berkeley, CA 94720-3860, USA*
[5]*Department of Physics and Astronomy, University of North Carolina, Chapel Hill, NC 27599-3255, USA*
[6]*Department of Physics, The George Washington University, Washington, DC 20052, USA*
[7]*INAF – Brera Astronomical Observatory, E. Bianchi 46, I-23807 Merate (Lc), Italy*
[8]*Astrophysics Research Institute, Liverpool John Moores University, Birkenhead CH41 1LD, UK*
[9]*Faculty of Mathematics and Physics, University of Ljubljana, Jadranska 19, SI-1000 Ljubljana, Slovenia*
[10]*Centre of Excellence SPACE-SI, Aškerčeva 12, SI-1000 Ljubljana, Slovenia*
[11]*Dark Cosmology Centre, Juliane Maries Vej 30, DK-2100 Copenhagen O, Denmark*

Accepted 2014 February 19. Received 2014 January 31; in original form 2013 May 8

ABSTRACT

We present broad-band observations and analysis of *Swift* gamma-ray burst (GRB) 120119A. Our early-time afterglow detections began under 15 s after the burst in the host frame (redshift $z = 1.73$), and they yield constraints on the burst energetics and local environment. Late-time afterglow observations of the burst show evidence for a moderate column of dust ($A_V \approx 1.1$ mag) similar to, but statistically distinct from, dust seen along Small Magellanic Cloud sightlines. Deep late-time observations reveal a dusty, rapidly star-forming host galaxy. Most notably, our early-time observations exhibit a significant red-to-blue colour change in the first ∼200 s after the trigger at levels heretofore unseen in GRB afterglows. This colour change, which is coincident with the final phases of the prompt emission, is a hallmark prediction of the photodestruction of dust in GRB afterglows. We test whether dust-destruction signatures are significantly distinct from other sources of colour change, namely a change in the intrinsic spectral index β. We find that a time-varying power-law spectrum alone cannot adequately describe the observed colour change, and allowing for dust destruction (via a time-varying A_V) significantly improves the fit. While not definitively ruling out other possibilities, this event provides the best support yet for the direct detection of dust destruction in the local environment of a GRB.

Key words: gamma-ray burst: individual: GRB 120119A – dust, extinction.

1 INTRODUCTION

More than 7 yr after the launch of *Swift* (Gehrels et al. 2004), a rich collection of optical light curves of gamma-ray bursts (GRBs) has been amassed. While global similarities in light-curve behaviours are becoming well established (e.g. Kann et al. 2010, 2011), thorough studies of individual bursts nevertheless continue to yield important insights into the details of the explosions and their environments. In particular, there remain relatively few examples of very early-time optical light curves when the prompt phase of the high-energy emission is still ongoing (for some examples, see Melandri et al. 2008; Panaitescu & Vestrand 2008;

⋆ E-mail: amorgan@astro.berkeley.edu
† Deceased 2011 December 12.

Cenko et al. 2009; Oates et al. 2009; Rykoff et al. 2009) due to the small but significant delays in relaying positional information to the ground, and the non-zero response times of even the fastest robotic telescopes.

Furthermore, the majority of the earliest time light curves are of a single colour (often unfiltered), which can provide only limited information on the evolution of the GRB emission and interactions with its surrounding environment. Contemporaneous, multicolour observations are needed to identify and characterize any colour change that may occur in the early afterglow.

Strong colour change is expected to occur for at least some events owing to the photodestruction of dust in the nearby environment of GRBs at early times (Waxman & Draine 2000; Draine & Hao 2002). Given the association of massive-star progenitors with long-duration GRBs, it is natural to expect GRBs to explode in dusty environments. However, only a small fraction (∼25 per cent) exhibits evidence for significant ($A_V > 1$ mag) dust obscuration in late-time optical/ultraviolet (UV) spectral energy distributions (SEDs; Covino et al. 2013). One potential explanation of this apparent discrepancy is the photodestruction of dust in GRB environments by prompt high-energy emission.

So far, however, unambiguous evidence for or against dust destruction in early GRB afterglows has been varied and inconclusive. As the bulk of the destruction is likely produced by bright X-rays during the prompt emission, optical observations contemporaneous with the high-energy radiation are needed in order to observe time variability in the SED (e.g. Fruchter, Krolik & Rhoads 2001; Perna, Lazzati & Fiore 2003).

Indirect evidence for or against dust destruction has been explored in observations of a few individual GRBs. In GRB 030418, an optical rise following a dearth of emission seen in images beginning ∼200 s after the start of the burst (>1 min after the prompt phase ended, and thus after dust destruction would have occurred) is interpreted as absorption of optical photons by dust inside a massive stellar wind medium (Rykoff et al. 2004). In this interpretation, complete destruction of the local dust did not occur, as some must have persisted to produce the attenuation. However, other models can be invoked to explain this early rise and subsequent decay that is now commonly seen in early-time optical afterglows (see e.g. Section 3.5).

In the case of GRB 061126, Perley et al. (2008a) and Gomboc et al. (2008) explore the possibility that grey dust could explain the observed deficit of optical flux to X-rays at late times. The optical dimness of this event was interpreted as optical absorption without the expected reddening by normal dust observed in the local Universe. While the presence of grey dust was not conclusively seen, a possible interpretation of its existence would be the sublimation of smaller grains in the local environment due to early photoionization of dust by the prompt X-ray emission. However, a significant change of A_V was not reported, so the grey dust might have been pre-existing.

In order to unambiguously identify the signatures of dust destruction, simultaneous, multicolour imaging of the afterglow (especially during the high-intensity high-energy emission) is necessary. With well-sampled, multicolour optical/near-infrared (NIR) observations beginning less than 1 min after the burst trigger, GRB 120119A offers one of the best cases yet to study the nature of an early-time GRB afterglow. The afterglow exhibits an appreciable red-to-blue colour change coincident with the end of the prompt high-energy emission, making this event an excellent candidate to test for the signatures of dust destruction. However, careful modelling of the SED as a function of time is needed to disambiguate between changes in the dust-absorption properties and other sources of colour change, such as a change in the intrinsic spectral index β.

In this study, we present observations and analysis of the broad-band afterglow of GRB 120119A. Details of the observations and data reduction are given in Section 2. Next, we present modelling and analysis, including general properties of the afterglow behaviour in Section 3.1, modelling of the late-time extinction profile in Section 3.2, details of the construction of early-time SEDs in Section 3.3, modelling of the early-time colour change in Section 3.4, constraints on the origin of the early emission in Section 3.5, and details of the host-galaxy properties in Section 3.6. To conclude, we discuss the implications of the results in Section 4. Throughout the paper we adopt the specific flux convention of $F(\nu, t) \propto \nu^{\beta} t^{\alpha}$. All quoted uncertainties are 1σ unless stated otherwise, and dates and times are given in UT.

2 OBSERVATIONS

2.1 *Swift* observations

GRB 120119A triggered the Burst Alert Telescope (BAT; Barthelmy et al. 2005) onboard *Swift* (Gehrels et al. 2004) at 04:04:30.21. *Swift* slewed immediately to the source and began observations with the X-Ray Telescope (XRT; Burrows et al. 2005) and Ultraviolet/Optical Telescope (UVOT; Roming et al. 2005) at 53.3 and 61 s after the trigger, respectively.

We processed the BAT data using the formalism of Butler et al. (2007). The BAT data show a duration of $T_{90} = 70 \pm 4$ s and a total fluence (15–350 keV) of $S = (2.3 \pm 0.1) \times 10^{-5}$ erg cm^{-2}. The XRT data were reduced using the pipeline described by Butler & Kocevski (2007), and they were corrected for Galactic neutral hydrogen (assuming the standard associated absorption from other elements) using the maps of Kalberla et al. (2005). The XRT bandwidth covers the energies 0.2–10 keV; all flux values quoted herein are converted to an effective energy of 1 keV.

The beginning of the XRT observations marginally overlaps with the end of the observed BAT emission; this initial steep decline of X-ray emission ($\alpha = -2.71 \pm 0.09$) is consistent with an extrapolation of the tail of the BAT emission to lower energies, as has been seen in many previous bursts (e.g. O'Brien et al. 2006).

The optical afterglow was clearly detected with the white filter onboard the UVOT in the initial finding-chart exposure taken ∼140 s after the burst ($m_{\rm white} = 19.5 \pm 0.1$ mag), and was again marginally detected in the B band ∼1800 s after the trigger ($B = 19.4 \pm 0.3$ mag; Chester & Beardmore 2012). It was undetected in all other filters, including the first U-band exposure ∼290 s after the trigger ($m_U > 18.7$ mag).

2.2 PROMPT observations

Observations of GRB 120119A were taken by the Skynet robotic telescope network using five Panchromatic Robotic Optical Monitoring and Polarimetry Telescopes (PROMPT) at Cerro Tololo Inter-American Observatory (CTIO) in Chile. Observations began at 04:05:08, 38 s after the burst. Observations in I, R, V, B, and open filters were taken beginning at different starting times, but nearly simultaneous multicolour observations were performed when possible. Unfortunately, the images take in the V band suffered from a previously unknown detector issue, and thus were not used in the analysis. The exposure of each observation increases with time since the GRB, with a minimum of 5 s to a maximum of 80 s in the I, R, B, and open filters. Additional late-time exposures were

Table 1. Photometry of GRB 120119A.

Instrument (UT)	Filter	$t_{\rm mid}$[a] (s)	Exposure time (s)	Magnitude[b]	Mag. uncertainty
KAIT	Clear	299.00	20.0	16.96	0.07
KAIT	Clear	399.00	20.0	17.02	0.09
KAIT	Clear	498.00	20.0	16.87	0.06
KAIT	Clear	598.00	20.0	16.76	0.10
KAIT	Clear	698.00	20.0	16.75	0.06
KAIT	Clear	796.00	20.0	16.75	0.07
KAIT	Clear	896.00	20.0	16.70	0.07
KAIT	Clear	995.00	20.0	16.68	0.07
KAIT	Clear	1095.00	20.0	16.95	0.06
KAIT	Clear	1195.00	20.0	17.04	0.06

Note. This table is published in its entirety in the electronic edition of MNRAS. A portion is shown here for guidance regarding its form and content.
[a]Time since the *Swift* trigger of the midpoint of the exposure.
[b]Magnitudes in this table have not been corrected for Galactic extinction ($E(B-V) = 0.093$ mag). Observations in the g', r', i', and z' bands are reported on the AB magnitude system. *B*-, *V*-, *R*-, *I*-, *J*-, *H*-, and *K*-band observations are referenced to Vega.

obtained with the Sloan g' and z' filters. Stacking is done manually as necessary to increase the signal-to-noise ratio (S/N), with an aim of obtaining photometric uncertainties of approximately ± 0.1 mag.

Photometry was performed using a custom pipeline written in C and PYTHON, based upon IRAF[1] aperture photometry. Photometric calibration was performed using a selection of seven Sloan Digital Sky Survey (SDSS) stars. For filters not in SDSS, colour transformations were performed using the prescription of Jester et al. (2005). The results are shown in Table 1, where magnitudes are in the Vega system.

2.3 PAIRITEL observations

The robotic Peters Automatic Infrared Imaging Telescope (PAIRITEL; Bloom et al. 2006) began automatic observations of GRB 120119A at 04:05:23, 53 s after the BAT trigger. PAIRITEL consists of the 1.3-m Peters Telescope at Mt. Hopkins, AZ, which was formerly used for the Two Micron All Sky Survey (2MASS; Skrutskie et al. 2006) but was subsequently refurbished with the southern 2MASS camera. PAIRITEL uses two dichroics to image in the NIR J, *H*, and $K_{\rm s}$ filters simultaneously every 7.8 s. Three images are taken at each dither position and then median combined into 23.4 s 'triplestacks'. Images are then resampled to 1 arcsec pixel^{-1} from its native 2 arcsec pixel scale and co-added using SWARP (Bertin et al. 2002).

Aperture photometry was performed using custom PYTHON software, utilizing Source Extractor (SEXTRACTOR; Bertin & Arnouts 1996) as a back end. The optimal aperture of 5.5 arcsec diameter was determined by minimizing the absolute error relative to 2MASS magnitudes of our calibration stars. Calibration was performed by redetermining the zero-point for each image individually by comparison to 2MASS magnitudes with the calibration stars. The resulting statistical uncertainty in the zero-point is negligible relative to other sources of error. Additional, systematic sources of error are addressed in detail by Perley et al. (2010); we use a similar procedure here to determine the total uncertainty of each point. The results are shown in Table 1, where magnitudes are in the Vega system.

2.4 KAIT observations

The Katzman Automatic Imaging Telescope (KAIT; Filippenko et al. 2001) began observations of GRB 120119A at 04:06:33, 2.05 min after the BAT trigger. KAIT is a 0.76-m telescope located at Lick Observatory dedicated to discovering and observing supernovae and other transients; it has been autonomously responding to GRB triggers since 2002 (Li et al. 2003b).

KAIT began observations by cycling through 20 s exposures in *V*, *I*, and unfiltered images, later switching to alternating *I* and unfiltered exposures, and finally (when the source was faint) just unfiltered images. Automatic bias subtraction and flat-fielding is performed at the telescope. Co-addition with SWARP is then performed as necessary to obtain significant detections of the afterglow.

Aperture photometry with a 2 arcsec radius was performed on the co-added images via a custom IDL wrapper based on the Goddard Space Flight Center (GSFC) IDL Astronomy User's library APER routine. Calibration was done relative to field stars from the SDSS Data Release 8 (DR8; Aihara et al. 2011), where magnitudes were converted into *V*, *R*, *I* using the transformation equations of Lupton (2005).[2] Unfiltered observations were calibrated relative to *R*-band magnitudes following the procedure of Li et al. (2003a). The results are shown in Table 1, where magnitudes are in the Vega system.

2.5 Liverpool observations

The 2-m Liverpool Telescope[3] (LT) robotically responded to the BAT trigger under its automatic GRB follow-up program (Guidorzi et al. 2006) and began observations ∼2.6 min after the burst. The first ∼10 min of observations were obtained with the RINGO2 polarimeter, which were co-added into a total of seven 80 s frames and then calibrated against the SDSS r' filter. Subsequent observations were acquired by alternating SDSS $r'i'z'$ filters from 14.5 to 53 min

[1] IRAF is distributed by the National Optical Astronomy Observatory, which is operated by the Association of Universities for Research in Astronomy (AURA), Inc., under cooperative agreement with the US National Science Foundation (NSF).

[2] http://www.sdss.org/DR7/algorithms/sdssUBVRITransform.html#Lupton2005

[3] http://telescope.livjm.ac.uk/

after the burst, with a pre-determined sequence of increasing exposures. Differential photometry was performed with respect to five SDSS field stars with the Graphical Astronomy and Image Analysis Tool (GAIA). The results are shown in Table 1, where magnitudes are in the AB system.

2.6 SMARTS observations

Beginning at 04:41:41 (∼0.64 h after the burst), data were obtained using the A Novel Dual Imaging Camera (ANDICAM) instrument mounted on the 1.3-m telescope at CTIO.[4] This telescope is operated as part of the Small and Moderate Aperture Research Telescope System (SMARTS) consortium.[5] The ANDICAM detector consists of a dual-channel camera that allows for simultaneous optical and IR imaging.

During each epoch, multiple dithered images were obtained with an image cadence designed to ensure that the final combined frames in each filter are referenced to the same time of mid-exposure. Thus, afterglow measurements are obtained at a single reference time for all filters, without any need for temporal extrapolation. Standard IRAF data reduction was performed on these images, including bias subtraction, flat-fielding, and sky subtraction. The images were then aligned and averaged to produce a single master frame for each epoch. During the first epoch, total summed exposure times equalled 180 s in *BRIJK* and 120 s in *HV*. For all other epochs, the total summed exposure times amounted to 15 min in *IV* and 12 min in *JK*.

The afterglow brightness was measured using seeing-matched, relative aperture photometry, with the relative magnitude of the afterglow determined by comparison with a set of field stars. The relative magnitudes were converted to apparent magnitudes by comparison with the Rubin 149 standard star (Landolt 1992) in the optical and with 2MASS stars in the IR.

2.7 P60 observations

We began observations of the afterglow of GRB 120119A with the automated Palomar 60-inch (1.5-m) telescope (P60; Cenko et al. 2006) beginning at 7:33 on 2012 January 19 (3.48 h after the *Swift*-BAT trigger). Images were obtained in the Sloan g', r', and i' filters, and individual frames were automatically reduced using our custom IRAF software pipeline. To increase the S/N, individual frames were astrometrically aligned using the SCAMP software package and co-added using SWARP (Bertin et al. 2002).

We used aperture photometry to extract the flux of the afterglow from these co-added frames with the aperture radius roughly matched to the full width at half-maximum (FWHM) of the point spread function (PSF). Aperture magnitudes were then calibrated relative to field sources from SDSS DR8. Imaging continued on the following night, but by then the afterglow had faded below our detection threshold. The results are shown in Table 1, where magnitudes are in the AB system.

2.8 Gemini-S spectroscopy

On January 19.20, 53 min after the BAT trigger, we utilized our rapid Target-of-Opportunity (ToO) program (GS-2011B-Q-9, PI: Cucchiara) to observe the optical afterglow with Gemini Multi-Object Spectrograph-South (GMOS-S) on the Gemini-South telescope. We obtained two spectra of 900 s each, with the R400 grating (corresponding to a resolving power of $R \approx 1200$ at 6000 Å) and a 1 arcsec slit, spanning the 4000–8000 Å wavelength range. Flat-field and Cu–Ar lamp calibration files were obtained immediately after the target observation.

The data were reduced using the GEMINI and GMOS packages available under the IRAF environment. Cosmic ray rejection was performed using the LACOS-SPEC routine (van Dokkum 2001). The extracted one-dimensional spectra were combined and normalized using the LONG_COMBSPEC, X_CONTINUUM, and X_NRMSPEC routine available under the XIDL package.

The final result is shown in Fig. 1. The spectrum reveals several metal absorption features, which are associated which a host galaxy at redshift $z = 1.728 \pm 0.05$. In addition, a strong Mg II system at lower redshift ($z = 1.212$) is present (as is common in GRB afterglow spectra; e.g. Prochter, Prochaska & Burles 2006; Cucchiara et al. 2009; Vergani et al. 2009).

2.9 Gemini-N observations

On January 21.28 (2.1 d after the burst) we observed the field of GRB 120119A with the GMOS (Hook et al. 2004) and Near Infrared Imager and Spectrometer (NIRI; Hodapp et al. 2003) as part of our rapid ToO program GN-2011B-Q-34 (PI: Tanvir) in order to continue monitoring the late-time behaviour of the afterglow. We performed a series of short (∼3 min) exposures in the optical g', r', and i' bands. These data were obtained with a dithered random pattern around the GRB location to improve the subsequent reductions. Data were flat-fielded and co-added using the GEMINI-GMOS tasks under the IRAF environment. The final co-added images consist of a total of 26 min (i') and 20 min (r' and g'), with a scale of 0.14 arcsec pixel^{-1}.

The IR observations consist of 20 dithered images of 80 s each (4 × 20 s exposures) in the J band, 18 dithered images of 80 s each (16 × 5 s exposures) in the H band, and 19 dithered images of 128 s each (16 × 8 s exposures) in the K band. Each sequence was obtained with dithering patterns similar to those for the GMOS data. Reduction, including cosmic ray rejection, flat-fielding, and co-addition, was performed using the NIRI package. The afterglow is detected in all of the final co-added images.

We obtained two additional NIRI K-band imaging epochs of the field of GRB 120119A using our standard ToO program (GN-2011B-Q-10, PI: Fox) on January 25 (∼6 d post-trigger) and April 2 (∼74 d post-trigger), with total integration times of 29 and 34 min, respectively. Seeing conditions were exceptional during both integrations (0.35 arcsec). Images were reduced and combined following the procedures above. In both of these co-adds we detect a faint, marginally extended (∼0.3″ arcsec), non-fading (<0.15 mag at 95 per cent confidence) source underlying the GRB position; we suggest that it is the GRB host galaxy.

2.10 Keck observations

We imaged the location of GRB 120119A with the Low Resolution Imaging Spectrometer (LRIS; Oke et al. 1995) on the Keck-I 10, telescope at three different epochs. The first epoch was carried out on January 26 between 10:42 and 11:07 (7.3 d post-trigger) with the g, R, and I filters. While seeing conditions for most of that night were generally poor, these data were taken within a brief window of good seeing (∼0.7 arcsec). An object is well detected at the

[4] http://www.astronomy.ohio-state.edu/ANDICAM
[5] http://www.astro.yale.edu/smarts

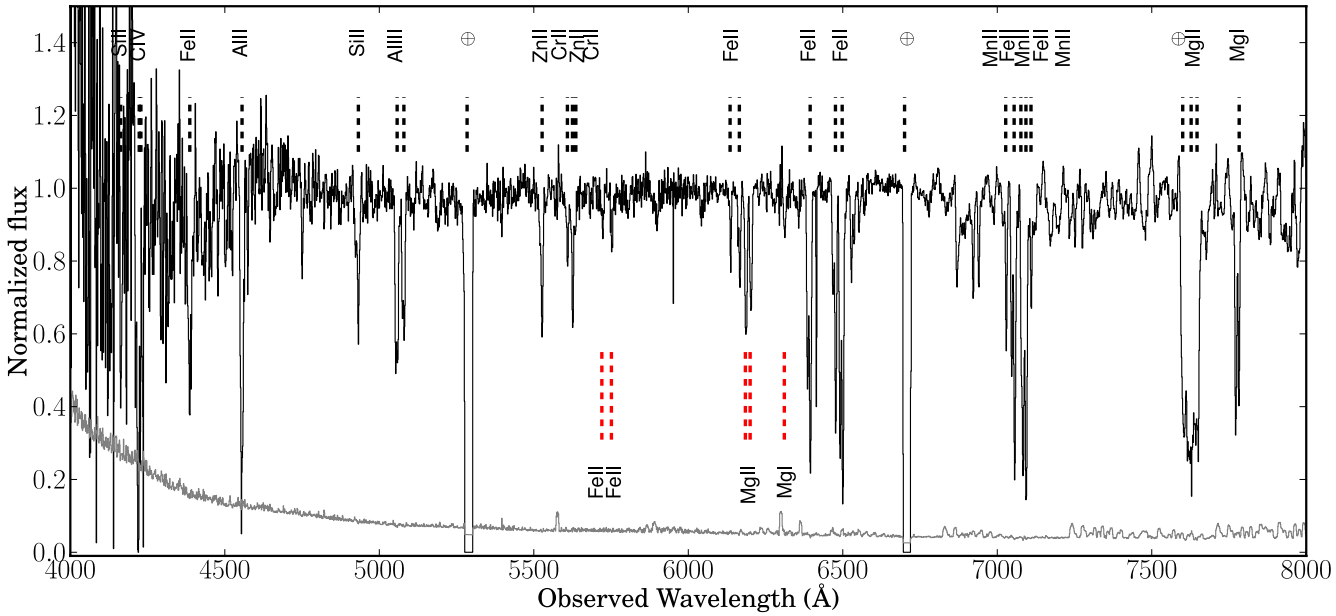

Figure 1. Normalized, combined spectrum of GRB 120119A obtained with GMOS-S. Two systems of absorption features are clearly identified. Indicated in black are the host-galaxy ($z = 1.728$) metal lines, while in red we see a strong Mg II absorber at $z = 1.212$, based on Mg II and Fe transitions. At the bottom, we show the noise spectrum.

afterglow position at a magnitude only slightly fainter than in the GMOS imaging several days earlier.

A second epoch of imaging was taken on February 21 (33 d post-trigger), but seeing conditions were poor (1.7 arcsec) and the position of the GRB is blended with the neighbouring galaxy 3 arcsec to the south. Nevertheless, a source is still clearly present at the GRB location. Photometry of this object was complicated by the poor seeing and blending, but we do not see any clear evidence of fading from the previous LRIS epoch.

A final epoch of imaging was performed on 2012 December 11 (0.89 yr after the burst) under relatively good seeing conditions (∼1.0 arcsec). Images were taken with the *B*, *R*, and *RG850* (roughly z') filters. The host galaxy is clearly detected in all three bands.

2.11 *Hubble Space Telescope* observations

The position around GRB 120119A was observed in the NIR with the Wide Field Camera 3 (WFC3) on the *Hubble Space Telescope* (*HST*) as part of our Cycle 20 program (GO-12949, PI: D. Perley) to investigate the host galaxies of dust-obscured GRBs. Observations were obtained in the *F125W* (wide *J*) and *F160W* (wide *H*) filters on 2012 October 28 (∼283 d post-trigger). The exposure time totalled 1209 s in each filter, taken in both cases at three dithered positions.

We downloaded the reduced observations from the Hubble Legacy Archive. The host-galaxy candidate from our Keck and Gemini observations is clearly extended (see Section 3.6). It is easily detected (S/N ≈ 30) in both frames, and it shows a morphology consistent with a bright, compact core ($r < 0.3$ arcsec) surrounded by a disc of lower surface brightness ($r \approx 0.8$ arcsec). There is no clear evidence of tidal features or ongoing interaction.

Photometry of the host galaxy was performed using a custom IDL aperture photometry routine using a circular aperture of 1.0 arcsec radius centred on the host position. We used the zero-points in the WFC3 handbook and aperture corrections of 0.07 mag (*F125W*) and 0.09 mag (*F160W*) measured from stars elsewhere in the images. The corresponding AB magnitudes of the host galaxy are $F125W = 23.13 \pm 0.04$ mag and $F160W = 23.34 \pm 0.07$ mag.

2.12 CARMA millimetre observations

We observed the location of GRB 120119A with the Combined Array for Research in Millimeter-wave Astronomy (CARMA) for 2.2 h on 2012 January 19, beginning at 11:47:42. The observation was undertaken at a frequency of 95 GHz with a bandwidth of 8 GHz, while the telescope was in the C configuration. We used the compact source J0744−064 as a phase calibrator and observed Mars for flux calibration. The data were reduced using the MIRIAD software.[6] The mid-epoch of the CARMA observation, ∼8.9 h since the burst, is close to the last optical/NIR observations that yielded a detection (at $t \approx 5.6$ h since the burst; see Fig. 2). The 3σ upper limit derived from the CARMA non-detection is 0.99 mJy at 95 GHz.

3 ANALYSIS

3.1 Optical/NIR light curve

A complete list of our afterglow photometry (uncorrected for Galactic extinction) is presented in Table 1. All flux values used for modelling in this work have been corrected for the expected Galactic extinction of $E(B - V) = 0.093$ mag along the line of sight using the dust maps of Schlegel, Finkbeiner & Davis (1998) and correcting for the ∼14 per cent recalibration of these maps reported by Schlafly & Finkbeiner (2011). The first day of optical/NIR photometry is plotted in Fig. 2, and some features are easily apparent. First, a significant red-to-blue colour change is observed during the first 200 s after the trigger. We note that the bulk of this colour evolution occurs coincident with the end of the prompt high-energy emission (see Fig. 3). We explore the details and implications of this colour change in Section 3.4.

[6] http://bima.astro.umd.edu/miriad/

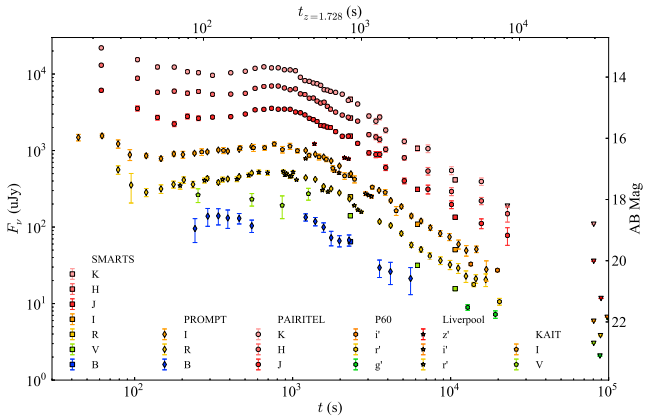

Figure 2. First-day optical/NIR light curve of GRB 120119A. A significant red-to-blue colour change is observed during the first 200 s after the trigger. An achromatic rise is seen around 800 s after the trigger, followed by some mild undulations before settling to a single power-law decay with index $\alpha_{\rm oir} = -1.30 \pm 0.01$. Unfiltered data are not included in this plot. The upper and lower time-axis scales refer to the rest frame and the observed frame, respectively.

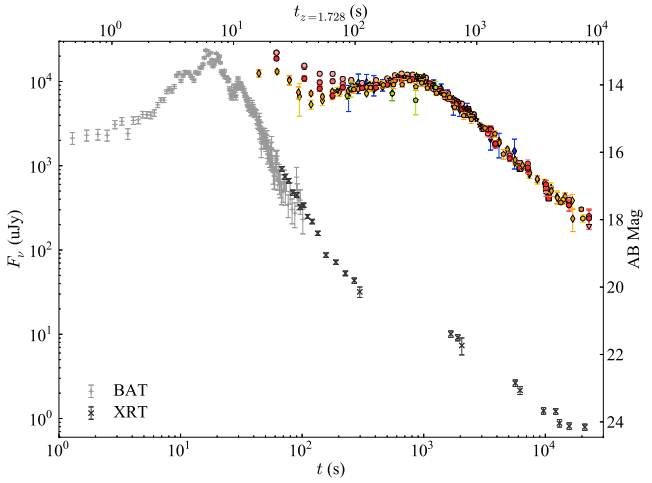

Figure 3. XRT light curve highlighting the overlap between the initial high-energy X-ray emission and the beginning of the optical observations during which significant colour change is seen for the first 200 s. The optical/NIR observations have all been scaled to the $K_{\rm s}$ band based on their late-time SED (Section 3.2) to highlight the early-time colour change. The optical/NIR markers are the same as in Fig. 2. The BAT data have been scaled up to match the XRT and are consistent with an extrapolation of the tail of the prompt BAT emission to lower energies. The upper and lower time-axis scales refer to the rest frame and the observed frame, respectively.

After the significant colour change ceased, the afterglow is seen to achromatically rise, peaking at roughly 800 s (observer frame). Minor oscillations are seen in some features during this peak, though coverage is limited and detailed modelling of these features is not presented here. We will explore the implications of the optical rise in Section 3.5.

The XRT afterglow (plotted in Fig. 3) is well fit by a series of power-law decays. The afterglow is initially caught in a rapid decay which is consistent with a lower energy extension of the tail end of the prompt gamma-ray emission seen by the BAT. The light curve then slows to a shallower decay of $\alpha_{\rm X} = -1.27 \pm 0.02$ by the onset of the second epoch of observations. To compare this afterglow with

Table 2. GRB 120119A afterglow SED.

Filter	Flux[a] (μJy)	1σ uncertainty (μJy)
B	45.0	2.5
V	109.9	5.0
r'	160.6	6.6
R	193.7	8.2
i'	340.6	15.9
I	456.1	19.2
z'	654.0	26.2
J	1358.6	44.9
H	2522.7	80.8
K	4312.1	144.5

[a]Afterglow fluxes were extrapolated to $t = 38.7$ min after the burst using our light-curve model. Values have not been corrected for Galactic extinction.

that at lower energies (Fig. 3), we fit the optical/NIR light curve from the time of the onset of the second epoch of XRT observations until the end of the early-time optical observations (∼0.4–5.6 h after the burst). While a single power-law component appears to dominate the light curve at this time, an additional excess of emission is seen at early times. We fit the light curve using a combination of a single power law plus a Beuermann et al. (1999) component (see Perley et al. 2008b, for a description of our light-curve fitting code). The power-law component has a decay index $\alpha_{\rm oir} = -1.30 \pm 0.01$, consistent with the XRT decay at this time, indicating that the flux originates from the same synchrotron spectral component. The minor rising component had a fixed rising index of $\alpha_{1,a} = 1.0$, and a best-fitting decay of $\alpha_{1,b} = 3.9 \pm 0.2$.

3.2 Late-time SED and extinction profile

At the time of the onset of the second epoch of XRT observations ∼20 min after the burst, the complex evolution of the light curve ceased and given way to a simple power-law decay as the primary emission component (Section 3.1). At this late stage, no evidence for further significant colour change is seen. To construct an SED from which to model the late-time dust extinction, we extracted the flux values in each band from our light-curve fit (Section 3.1) to the time of the first SMARTS observation 38.7 min post-burst. The resultant 1σ uncertainties on the fit parameters were multiplied by $\sqrt{(\chi^2/{\rm dof})}$ for each corresponding filter to weight the uncertainty in each colour by an estimate of the individual light-curve fit qualities (which is particularly important for the z and V bands because of the relatively small number observations in these filters). Estimated systematic uncertainties of 0.03 mag in the NIR and 0.04 mag in the optical were then added in quadrature. The resultant SED is given in Table 2 and plotted in Fig. 4.

The SED clearly shows a significant dust component. We fit various extinction laws to the SED using a custom PYTHON implementation of the Fitzpatrick (1999) parametrization based upon the GSFC IDL Astronomy User's library. Average parameter values were extracted from Gordon et al. (2003) for the Small Magellanic Cloud (SMC) and Misselt, Clayton & Gordon (1999) for the Large Magellanic Cloud (LMC). Flux values and colours were corrected for the observed redshift ($z = 1.728$; Section 2.8) and Galactic extinction [$A_{\rm V} = 0.288$ mag, assuming $R_{\rm V} = 3.1$ for the Milky Way (MW)],

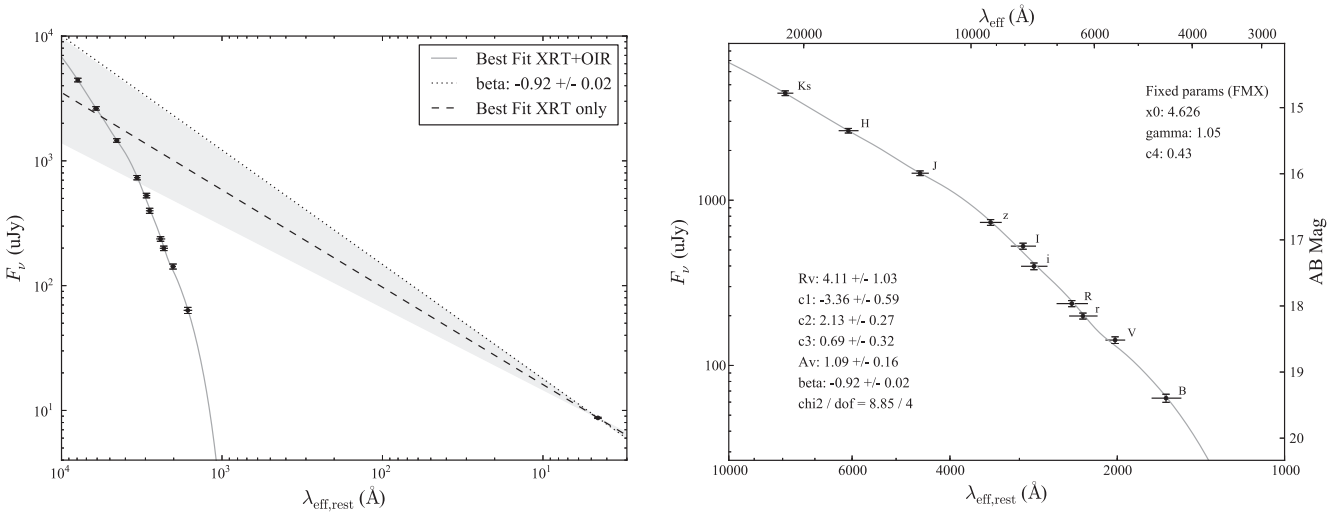

Figure 4. Late-time SED of GRB 120119A inferred from our light-curve model extrapolated to 38.7 min after the burst (Table 2). Values were corrected for the host redshift ($z = 1.728$) and Galactic extinction ($A_{\rm V} = 0.288$ mag). Left-hand panel: the dashed line and light grey cone represent the best-fitting value and uncertainty (respectively) of β inferred from the XRT spectrum alone using the products of Butler & Kocevski (2007): $\beta_{\rm xrt} = 0.78 \pm 0.12$. The solid grey curve shows the best-fitting dust model (FMX; χ^2/dof = 8.9/4), and the dotted line is the β inferred from that fit. Right-hand panel: zoomed in SED highlighting the optical/NIR points. The horizontal bars at each point show the FWHM of the corresponding filter. The solid grey curve shows the best-fitting dust model (FMX).

Table 3. Results of extinction fits.

Dust model	+XRT?	β	$A_{\rm V}$ (mag)	χ^2/dof
LMC	N	-2.05 ± 0.11	0.37 ± 0.07	135.8/7
LMC	Y	-0.92 ± 0.00	1.14 ± 0.01	230.1/8
LMC2	N	-1.03 ± 0.16	1.09 ± 0.11	69.5/7
LMC2	Y	-0.92 ± 0.00	1.16 ± 0.01	70.0/8
MW	N	-2.50 ± 0.09	0.07 ± 0.06	160.5/7
MW	Y	-0.94 ± 0.00	1.26 ± 0.02	464.6/8
SMC	N	-1.39 ± 0.11	0.62 ± 0.06	23.5/7
SMC	Y	-0.89 ± 0.00	0.88 ± 0.01	44.0/8
FM	N	-1.04 ± 3.27	0.97 ± 3.26	8.9/3
FM	Y	-0.92 ± 0.02	1.09 ± 0.16	8.9/4

and the intrinsic spectral index β was allowed to be free in all fits. The resultant fits are shown in Table 3.

Of the three standard local dust extinction laws (MW, LMC, SMC), the SED is by far best fit by an SMC curve (χ^2/dof = 23.5/7), using the average value of the ratio of total to selective extinction $R_{\rm V} = 2.74$ from Gordon et al. (2003). Fits with $R_{\rm V}$ as a free parameter were attempted, but lacking UV detections this parameter could not be well constrained. For SMC dust, the best-fitting values for extinction and spectral index are $A_{\rm V} = 0.62 \pm 0.06$ mag and $\beta = -1.39 \pm 0.11$.

We can further constrain the value of β by including the interpolated, unabsorbed XRT flux in the SED fit ($E_{\rm xrt,\,eff} = 1$ keV; see Section 2.1). We note that the resultant best-fitting value of β from the optical/NIR data alone is somewhat large for this stage in the evolution and is inconsistent with the XRT observations under the assumption of a synchrotron-emission origin (e.g. Sari, Piran & Narayan 1998). As the X-ray and optical/NIR afterglows are fading at approximately the same rate at the SED extrapolation time ($\alpha_{\rm X} = -1.27 \pm 0.02$, $\alpha_{\rm oir} = -1.30 \pm 0.01$; see Section 3.1), we can assume they originate from the same component of the synchrotron spectrum. With the inclusion of the XRT data in the SMC dust fit, we obtain best-fitting values of $A_{\rm V} = 0.88 \pm 0.01$ mag and $\beta = -0.89 \pm 0.01$.

That the SMC curve gives the best fit among the standard dust laws is consistent with the findings of previous studies (e.g. Schady et al. 2012; Covino et al. 2013). However, the goodness of fit is still poor (χ^2/dof = 44.0/8) given the quality of the data. We thus attempted a more general fit using the full parametrization of Fitzpatrick (1999), which is described by six parameters: c_1 and c_2 are (respectively) the intercept and slope of the linear part of the UV component in $E(\lambda - V)$, c_3 is the strength of the 2175 Å bump, c_4 is the strength of the rise in the far-UV, x_0 is the centroid of the 2175 Å bump in inverse microns ($x_0 \approx 1/0.2175$), and γ is the width of that feature.

The values of x_0 and γ are not seen to vary widely among dust sight lines within the Local Group, and thus we opt to keep these parameters fixed at $x_0 = 4.626$ and $\gamma = 1.05$. Furthermore, the c_4 parameter which gives the far-UV extinction curvature at wavelengths $\lambda < 1700$ Å is poorly constrained due to the lack of sufficiently blue filters in our data. As such, we fixed this parameter to the average value of $c_4 \approx 0.43$ found from the sample of Schady et al. (2012). All other parameters were allowed to vary freely. The resultant fits are shown in Table 4. While the parameter values without the XRT data included in the fit are poorly constrained, the best-fitting dust law including the X-ray flux (henceforth FMX) shows a marked improvement over the other extinction laws (χ^2/dof = 8.85/4; Table 3). The best-fitting FMX curve is shown in Fig. 4 and yields values of $A_{\rm V} = 1.09 \pm 0.16$ mag and $\beta = -0.92 \pm 0.02$.

The best-fitting FMX curve indicates that a weak 2175 Å bump may be present ($c_3 = 0.69 \pm 0.32$), which at $z = 1.728$ would lie nearly coincident with our R-band observations. However, it is of marginal significance, and re-fitting the SED after fixing the bump strength as zero produces no appreciable difference in the best-fitting values of the other parameters nor the overall quality of fit. Further, no evidence for this feature is seen in our Gemini spectrum (Fig. 1). This feature has been more securely detected in several other GRBs, such as GRB 070802 (Krühler et al. 2008; Elíasdóttir et al. 2009), GRB 080603A (Guidorzi et al. 2011), GRB 080605

Table 4. Best-itting (Fitzpatrick 1999) dust parameters for GRB 120119A.

Dust model	A_V (mag)	β (s)	R_V (mag)	c_1	c_2	c_3	c_4	χ^2/dof
FM	0.97 ± 3.26	−1.04 ± 3.27	4.13 ± 1.32	−3.76 ± 12.17	2.29 ± 4.91	0.75 ± 1.82	0.43(fixed)	8.9/3
FMX	1.09 ± 0.16	−0.92 ± 0.02	4.11 ± 1.03	−3.36 ± 0.59	2.13 ± 0.27	0.69 ± 0.32	0.43(fixed)	8.9/4

(Zafar et al. 2012), GRB 080607 (Perley et al. 2011), and GRB 080805 (Zafar et al. 2012).

The closure relations of standard afterglow theory (e.g. Granot & Sari 2002; Piran 2005) can be used to infer the temporal decay index α and spectral index β under various conditions through their relations with the electron spectral index p, allowing for a consistency check of our derived values for these two parameters. Under the assumption of an adiabatic expansion of the blast wave into a homogeneous external medium (n = constant) in the slow-cooling regime, there are two possibilities for the spectral index β in the temporally decaying part of the light curve: $\beta = -(p-1)/2$ for $\nu_m < \nu < \nu$, and $\beta = -p/2$ for $\nu_c < \nu$. The two possible values for α in these regimes are $\alpha = -3(p-1)/4$ and $\alpha = -3(p-2)/4$, respectively, leading to the closure relations $\beta = 2\alpha/3$ for ν between the peak frequency and the cooling break, and $\beta = 2(\alpha-1)/3$ for $\nu > \nu_c$. Adopting $\alpha \approx -1.30$ at the SED extrapolation time, we derive $\beta \approx -0.87$ for the $\nu_m < \nu < \nu_c$ closure relation, consistent with our more secure determination of $\beta = -0.92 \pm 0.02$ from the SED fit. In this interpretation, the cooling break has not yet passed through our bandpasses and the electron energy distribution index is $p \approx 2.7$.

We can further check our derived value of A_V by comparing it to the neutral hydrogen absorption excess as derived from X-ray data. Using the photon-counting (PC) mode data from the XRT, we measure $N_H = 1.03^{+0.46}_{-0.39} \times 10^{22}$ cm^{-2}. Watson & Jakobsson (2012) found that in addition to the general trend of a high A_V requiring large values of X-ray absorption (Schady et al. 2010), there is also a redshift trend indicating a dearth of low-z events with low A_V and high N_H. This was expanded recently by Covino et al. (2013). While there is significant scatter in this relation, our derived values of X-ray absorption and optical extinction are in general agreement with the N_H/A_V trend of events at similar redshifts.

3.3 Construction of early-time SEDs

Our early-time observations are from a variety of telescopes and filters, at irregular times, and often rather sparsely sampled. In order to model colour change as a function of time, we built up a series of SEDs at different temporal epochs using the PAIRITEL, PROMPT, Liverpool, and SMARTS photometry. PROMPT clear-filter observations were not included in the SED constructions due to complications in accurate colour corrections with a changing sky background, and approximate redundancy with the equally well-sampled R filter.

One option for exploring colour change as a function of time is to identify epochs where data through multiple filters were obtained nearly simultaneously. We explored this option, but coincident temporal alignment of images was only achievable six times within the first 20 min after the burst, leaving most of the data unused.

To circumvent this problem, interpolation was performed to create denser temporal sampling. Because the PAIRITEL observations had the highest time resolution, these were chosen for interpolation. We use a non-parametric light-curve estimate to interpolate the GRB brightness (and measurement errors) in epochs of incomplete photometric coverage. By using a flexible, non-parametric interpolation model, we avoid assuming an overly restrictive GRB template model and allow the data to determine the appropriate smooth light-curve shape.

To perform interpolation, we fit a natural cubic regression spline (Ruppert, Wand & Carroll 2003; Wasserman 2006) separately to the data from each of the three PAIRITEL bandpasses. We utilize regression splines because they are particularly adept at estimating smooth functions that may have complicated behaviour such as periods of rapid decline and allow a straightforward estimate of both the brightness and model uncertainty of the brightness at each interpolation epoch (see e.g. Richards et al. 2012 for usage in the context of supernova light curves). Using a cubic spline model, the estimate of the magnitude in photometric band b at time t is

$$\widehat{m}_b(t) = \sum_{j=1}^{N+4} \widehat{\beta}_b(t) B_j(t), \quad (1)$$

where N is the number of spline knots, B_j is the jth natural cubic spline basis, and the $\widehat{\beta}_b(t)$ are estimates of the spline coefficients that are found by minimizing the weighted least-squares statistic of the spline-model magnitudes against the observed magnitudes $m_b(t)$ with weights $(1/\sigma_b(t))^2$. Here, $\sigma_b(t)$ is the observational error in the measurement of $m_b(t)$.

When fitting a regression spline, one must choose the quantity, N, and the locations of the knots, which correspond to points of discontinuity of the third derivative of the interpolated spline function. In this work, we follow convention and place the knots uniformly over the observed time points, which have been converted to logarithmic space. To choose N, we pick the value that minimizes the generalized cross-validation (GCV) score, which balances the bias and variance of the fitted interpolation function with an explicit penalty to avoid overfitting to the observed data (see e.g. Richards et al. 2012). The GCV criterion is defined as

$$\mathrm{GCV}_b(N) = \frac{1}{n_b} \sum_{k=1}^{n_b} \left(\frac{m_b(t_k) - \widehat{m}_b(t_k)}{\sigma_b(t_k)(1 - N/n_b)} \right)^2, \quad (2)$$

where $\widehat{m}_b(t_k)$ is the fitted value, at time t_k, of a spline with N knots, computed using equation (1); $t_1, t_2, \ldots, t_{n_b}$ is the grid of epochs of observation in the light curve for photometric band b; and n_b is the number of observed epochs of the light curve. In this formulation, the observational uncertainties in the measured magnitudes, $\sigma_b(t_k)$, are used to compute both the interpolated light-curve magnitude estimates, $\widehat{m}_b(t)$, and the model uncertainty in those estimates. Using the GCV criterion, we search for the optimal number of spline knots over the range 1–50, finding the optimal value to be 14 for each of the J and H bands, and 8 for K_s.

The spline regression provides a model uncertainty for each interpolation point, which must be combined in quadrature with an estimate of what the photometric uncertainty would have been had an observation taken place at that time. To approximate the latter, we performed another spline fit to the photometric uncertainties for each PAIRITEL filter as a function of time, assuming that each photometric uncertainty (Section 2.3) itself was uncertain at roughly the

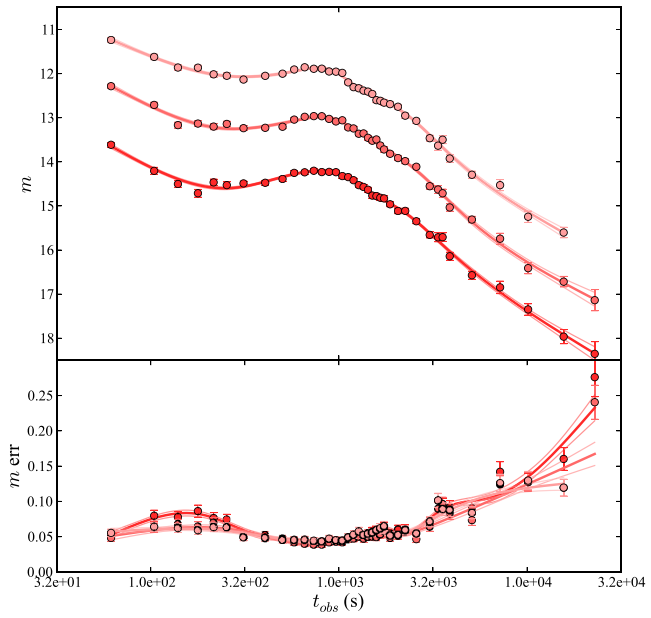

Figure 5. Natural cubic regression spline fits to the PAIRITEL data for use in interpolation. The upper plot shows the fit to the light curves, found via the GCV criterion to have an optimal number of 8 spline knots for K_s, and 14 for each of J and H. The bottom plot shows a fit to the photometric uncertainties, assuming each point was uncertain at the 10 per cent level, in order to estimate these values at the interpolation points. The central lines show the optimal model fit, and the lighter outer lines show the model uncertainty. The plot colours are the same as in Fig. 2.

10 per cent level. The resultant fit is shown in the bottom panel of Fig. 5; the optimal number of knots was 12, 6, and 7 for J, H, and K_s, respectively. For each interpolated point, the associated uncertainty at a particular point in time was the mean approximate instrumental uncertainty inferred from this interpolation added in quadrature with the model uncertainty at that time.

The end result of the interpolation is a series of 4–7 colour SEDs, finely sampled in time. While some bluer filters are occasionally included in these SEDs, the majority are five-colour $RIJHK_s$ SEDs from PROMPT and PAIRITEL. While these alone cannot strongly break the intrinsic degeneracy between A_V and β, the longer lever arm afforded by the more secure late-time SED (see Section 3.2) gives us strong constraints on both these parameters and the type of dust. These SEDs can now be used to model the colour change as a function of time.

3.4 Modelling colour change

The simplest way to model the colour change is to assume that the dust properties in the GRB environment are fixed and that only the spectral index β is causing the change. Each interpolated SED was fit under this assumption, with β left free and the dust parameters fixed at the inferred late-time values from the best-fitting dust extinction law (FMX; see Section 3.2). The parameter β is fit independently at each SED, and no constraints are imposed on how it is allowed to vary with time. The results are shown in the left-hand panel of Fig. 6.

A second possibility is that the colour change results from a superposition of two different emission components of different intrinsic spectral indices. In particular, a decaying reverse shock superimposed on a rising forward shock might qualitatively explain the observed features (as previously seen in GRBs 061126, 080319B, and 130427A; Perley et al. 2008a, 2014; Racusin et al. 2008; Bloom et al. 2009). We fixed the extinction to its late-time value and fit the light curve using the empirical model of Perley et al. (2008b), allowing the spectral indices of the early-time power-law component to differ from the late-time component. The fit at early times is poor and results in a spectral index change ($\Delta\beta = 0.93$) that is much larger than seen in previous reverse/forward shock transitions, and larger than expected by theory. The presence of a bright reverse shock is also disfavoured by the CARMA/Very Large Array (VLA) non-detections (Section 3.5).

We next explored whether time varying dust extinction signatures could be contributing to the colour change. The photodestruction of dust is expected to alter both the extinction A_V and selective reddening R_V (e.g. Perna et al. 2003). There is also the possibility that the dust in the local environment of the GRB that would be affected has a significantly different extinction signature than the dust causing the observed late-time absorption. For simplicity we

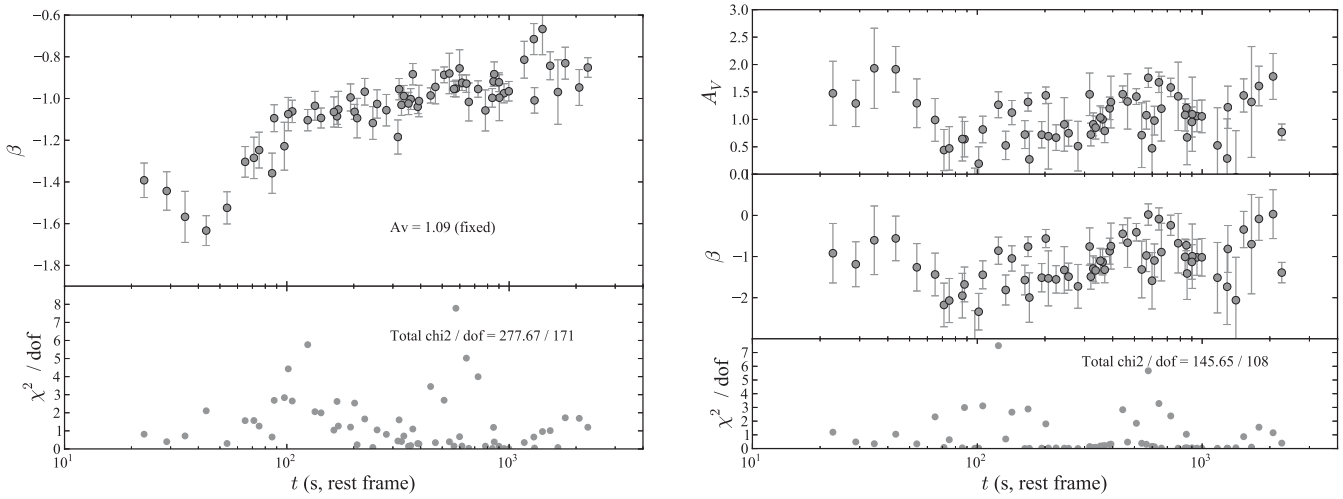

Figure 6. Left-hand panel: the best-fitting values of β for each interpolated SED as a function of time. The extinction A_V was fixed to the late-time value of 1.09 and FMX-like dust was assumed (see Section 3.2). Plotted below is the reduced χ^2 statistic for each individual fit. Right-hand panel: same as the left-hand panel, but where both A_V and β were allowed to vary freely.

Table 5. Results of colour change fits.

Dust model	$A_{V,0}$ (mag)	ΔA_V (mag)	τ_{A_V} (s)	β_0	$\Delta\beta$	τ_β (s)	χ^2/dof
LMC2	-1.16 (fixed)	0.47 ± 0.72	57.51 ± 63.09	-0.92 (fixed)	-0.33 ± 0.81	65.32 ± 121.31	587.5/230
SMC	-0.88 (fixed)	0.60 ± 0.10	44.19 ± 9.86	-0.89 (fixed)	-0.28 ± 0.05	513.56 ± 104.17	383.5/230
FMX	-1.09 (fixed)	0.61 ± 0.15	39.00 ± 13.34	-0.92 (fixed)	-0.28 ± 0.09	258.90 ± 71.18	365.6/230

search for a change in the dust parameters by allowing only A_V to change and keeping all other extinction parameters fixed.

We refit each interpolated SED, allowing both A_V and β to vary freely, under no constraints as to how they are allowed to vary as a function of time. The results are shown in the right-hand panel of Fig. 6; they exhibit a drastic change compared with the left-hand panel of this figure in both behaviour and overall quality of fit (total χ^2/dof = 146.7/108 versus χ^2/dof = 277.7/171). The fact that β alone is not the dominant source of colour change in this fit gives a preliminary indication that a decrease in absorption may be present.

However, as this simple illustration imposes no constraints regarding how the parameters are allowed to change, the variations in A_V and β between epochs are often unphysically large and rapid. To account for this, simple, monotonic functional forms for $A_V(t)$ and $\beta(t)$ were assumed:

$$A_V(t) = A_{V,0} + \Delta A_V e^{-t/\tau_{A_V}} \quad (3)$$

and

$$\beta(t) = \beta_0 + \Delta\beta e^{-t/\tau_\beta}. \quad (4)$$

In these parametrizations, $A_{V,0}$ and β_0 represent the late-time values of extinction and spectral index, and ΔA_V and $\Delta\beta$ correspond to the total change from the early-time values ($t = 0$). No change in the total amount of extinction would thus be consistent with $\Delta A_V = 0$. In these fits, ΔA_V was required to be positive; that is, we did not allow for an increase in extinction with time.

In fitting this model to the N SEDs constructed from M flux measurements as described in Section 3.3, we fixed the dust extinction model as well the late-time values of A_V and β inferred from that model for a variety of the late-time extinction curves shown in Table 3. In addition to the four remaining parameters ΔA_V, $\Delta\beta$, τ_{A_V}, and τ_β, a flux normalization parameter was fit for each SED, leading to a total of $M - (N + 4)$ degrees of freedom. The results are shown in Table 5. While the precise results are dependent on the assumed late-time extinction model, we note that in all cases, ΔA_V is found to be positive to a statistically significant level. In other words, under the model assumptions, dust destruction is favoured for each extinction law. The change in spectral index β, on the other hand, is less favoured as the dominant source of colour change, and its behaviour with time is more dependent on the assumed extinction law.

As with the fits to the late-time dust, the extinction model that yielded the best fit to the colour change was FMX, giving further support for this model over a simple SMC law. The behaviours of A_V and β with time using the best-fitting values from this model are presented in Fig. 7. To give a sense of the variance and covariance among the fit parameters, we drew 1500 samples from the resultant best-fitting multivariate normal distribution (light-grey curves) with confidence contours overplotted (dashed lines contain 68 per cent of the curves, dotted 95 per cent).

Unlike the degeneracy typically seen between A_V and β in dust-model fits to optical/NIR SEDs, the parameters describing the change in A_V and β with time (ΔA_V and $\Delta\beta$) exhibit only mild

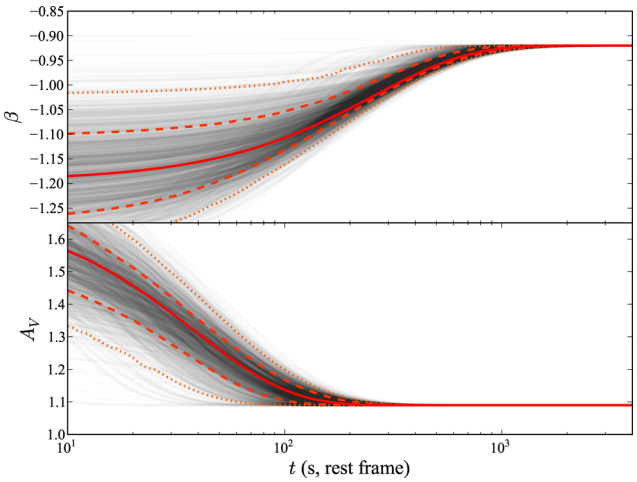

Figure 7. Best-fitting values for $A_V(t)$ (mag) and $\beta(t)$ according to the functional forms of equations (3) and (4), simultaneously fit to all available data at each SED interpolation point. FMX-type dust was assumed (Section 3.2). Light-grey lines show the resultant curve from one of the 1500 samples drawn from the multivariate normal distribution from the best-fitting model. The mean value is plotted in red, with confidence contours overplotted with dashed lines (containing 68 per cent of the curves) and dotted lines (containing 95 per cent of the curves).

covariance. After marginalizing over all other parameters the covariance is shown in Fig. 8. Subject to all of the model assumptions outlined above, extinction change is expected with about 4σ confidence, with a mean value of $\Delta A_V = 0.61 \pm 0.15$ mag.

To guard against the fit falling into a local minimum, we fit each model 1000 times to the data over a randomly selected set of initial conditions for each fit parameter over the following ranges: $0 \leq \Delta A_V \leq 2$ mag, $-2 \leq \Delta\beta \leq 0$, $0 \leq \tau_{A_V} \leq 1000$ s, and $0 \leq \tau_\beta \leq 1000$ s. Each initial normalization parameter value was also randomly selected from a range encompassing all possible physical values. The fits given in Table 5 had both the best fits (lowest χ^2) as well as the plurality of convergences for each presented dust model.

3.5 Optical rise and shock constraints

The colour-change modelling described in Section 3.4 was performed free from assumptions of an underlying light-curve model; each time slice was treated independently and was fit with flux normalization as a free parameter. The analysis above indicates that this colour change is likely caused at least in part by dust destruction (as will be discussed further in Section 4). As such, model-dependent absorption corrections would need to be performed in order to infer the intrinsic light curve, which itself could be produced by multiple emission components, including prompt emission from the central engine.

The second peak at ~800 s (observer frame) is more straightforward to interpret. The lack of significant colour change across

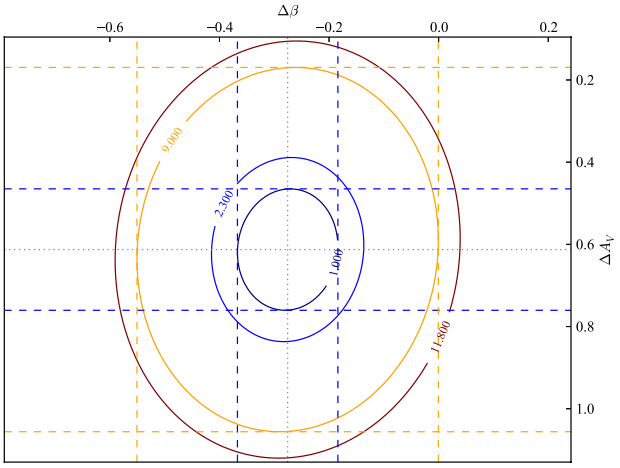

Figure 8. Covariance between parameters ΔA_V and $\Delta\beta$ from equations (3) and (4). These parameters correspond to the total change in the values of A_V and β over the course of the light curve (i.e. a value of $\Delta A_V = 0$ would be consistent with no change in the amount of dust). The outer blue ellipse ($\Delta\chi^2 = 2.3$) and the outermost red ellipse ($\Delta\chi^2 = 11.8$) show the 68.3 and 99.73 per cent confidence intervals for two degrees of freedom. The dotted blue and orange lines show the projections for a further marginalization to a single parameter of interest, corresponding to the 1σ and 3σ confidence intervals for ΔA_V and $\Delta\beta$ alone.

the peak immediately rules out some possibilities for the optical rise. For instance, the passage of the peak frequency ν_m of the forward-shock synchrotron emission through the observed bands would produce a temporal rise if it occurred after the initial fireball deceleration. However, this would result in a blue-to-red colour change as ν_m passes from high to low frequencies; for instance, for expansion into a homogeneous external medium in the slow-cooling regime, the intrinsic spectral index should pass from $\beta \approx \nu^{1/3}$ to $\approx\nu^{-(p-1)/2}$, where p is the electron energy index (Sari et al. 1998).

The achromatic steep rise and slow decay of the afterglow at this stage shows some of the hallmarks of the onset of the forward shock as the fireball sweeps through the external medium. If this is the reason for the peak, we can use the time of the peak to obtain an estimate of the initial Lorentz factor Γ. Following the methodology of Mészáros (2006) and Rykoff et al. (2009), and assuming a constant circumburst density profile such as that of the interstellar medium (hereafter 'ISM-like'), we have

$$\Gamma_0 \approx 2\Gamma_{\rm dec} = 2\left(\frac{3E_{\rm iso}}{32\pi n m_{\rm p} c^5 \eta t_{\rm pk,z}^3}\right)^{1/8} \approx 560\left(\frac{3E_{\rm iso,52}}{n_0\eta_{0.2}t_{\rm pk,z,10}^3}\right)^{1/8}. \quad (5)$$

In this equation, $E_{\rm iso,\,52}$ is the isotropic γ-ray energy release in units of 10^{52} erg, n_0 is the circumburst density in units of cm^{-3}, $\eta_{0.2} = \eta/0.2$ is the radiative efficiency, and $t_{\rm pk,\,z,\,10}$ is the rest-frame afterglow peak time in units of 10 s.

This determination requires an estimate of $E_{\rm iso}$, as derived from the spectral model of the gamma-ray data. For consistency with the analysis of Rykoff et al. (2009), we adopt the value of $E_{\rm iso}$ derived from the methodology of Butler et al. (2007), utilizing a Bayesian analysis with Burst and Transient Source Experiment (BATSE) spectral priors to estimate $E_{\rm iso}$ using the relatively narrow range of (15–150 keV) from the BAT. However, the estimate of Γ is only weakly dependent on $E_{\rm iso}$ (1/8th power), so the slightly different estimates (by a factor of <2) from *Konus-Wind* (Golenetskii et al. 2012) and *Fermi* Gamma-Ray Burst Monitor (GBM; Gruber 2012) does not significantly alter the result. Using $E_{\rm iso} = 2.1 \times 10^{53}$ erg and $t_{\rm pk,z} \approx 300$ s, we find $\Gamma_0 \approx 260(n_0\eta_{0.2})^{-1/8}$.

The redshift of GRB 120119A is comparable to that of GRB 990123 for which a bright radio flare from the reverse shock was detected. The reverse-shock emission observed for GRB 990123 peaked at ∼1 d since burst, at a flux level of ∼100–260 μJy (Galama et al. 1999; Kulkarni et al. 1999) in the GHz range. Our CARMA upper limit on GRB 120119A (Section 2.12) does not allow us to exclude a radio flare as bright as the one of GRB 990123. However, GRB 120119A was also observed with the Expanded Very Large Array (EVLA) beginning 2012 January 21.2 (2.0 d after the burst) at a mean frequency of 5.8 GHz (Zauderer & Berger 2012). No significant radio emission was detected to a 3σ upper limit of 34 μJy. This upper limit is below the ∼5 GHz flux of 164 ± 100 μJy measured by Galama et al. (1999) at ∼2 d since GRB 990123. A reverse-shock contribution as bright as the one observed in GRB 990123 is thus disfavoured in the case of GRB 120119A.

Hereafter, we check whether the CARMA upper limit can constrain the forward-shock parameters when combined with the optical-to-X-ray observations of GRB 120119A. The similarity of the optical/NIR and X-ray temporal slopes, starting from $\sim 3 \times 10^3$ s since the burst, suggests that the synchrotron frequency ν_m is below the optical/NIR band ($\nu_m \propto t^{-3/2}$; Sari et al. 1998), which allows for a determination of an upper limit on ν_m. A lower limit can be placed on ν_m by extrapolating the R-band optical flux to the time of the CARMA observation with our light-curve model (Section 3.1), under the assumption that the synchrotron self-absorption frequency ν_a is below the CARMA band at the time of our observation, using

$$F_{95\,\rm GHz} = F_{\rm opt}\left(\frac{\nu_{\rm opt}}{\nu_m}\right)^{-\beta_{\rm opt}}\left(\frac{\nu_m}{95\,\rm GHz}\right)^{-1/3} \lesssim 0.99\,\rm mJy. \quad (6)$$

This gives the bounds $5.49 \times 10^{11} < \nu_m < 4.07 \times 10^{12}$ Hz and $3.3 \times 10^2 < F_m < 1.8 \times 10^3$ μJy. In addition, since no strong evidence for a break is observed in the X-ray light curve up to ∼1 d since the burst, we can constrain the cooling-break frequency to be $\nu_c(1\,\rm d) \gtrsim 1$ keV.

These constraints can be used to make estimates of the circumburst density n, the fraction of energy imparted to swept-up electrons η_e, and the fraction of energy going into magnetic fields η_B. Using the formalism of Yost et al. (2003) and assuming an adiabatically expanding fireball and a constant (ISM-like) circumburst matter density, a solution satisfying our constraints (using $p = 2.7$ as estimated above) is $n \approx 0.1$ cm^{-3}, $\epsilon_B \approx 5 \times 10^{-4}$, and $\epsilon_e \approx 0.1$, consistent with values found for other *Swift* events (Liang et al. 2008; Melandri et al. 2010). We note, however, that this set of parameters would imply a slightly higher flux at the time and frequency of the EVLA observation (∼100 μJy) than the upper limit of Zauderer & Berger (2012), under the assumptions outlined above.

3.6 Host-galaxy properties

The detection of a non-fading, extended source coincident with the GRB afterglow days to months after the GRB indicates that we have detected the GRB host galaxy. Given the negligible offset and relative brightness of the source (<0.2 arcsec and $R = 24.8$ mag), we calculate a very small probability of chance coincidence: $P_{\rm chance} = 4 \times 10^{-3}$ (Bloom, Kulkarni & Djorgovski 2002).

The negligible fading in the K band relative to the late-time data (and only very marginal fading of the optical counterpart

Table 6. GRB 120119A host photometry.

Filter	Magnitude[a]	1σ uncertainty
B	25.50	0.13
g'	25.27	0.05
R	24.60	0.17
R	24.68	0.11
I	23.65	0.13
z'	24.12	0.13
K	20.91	0.13
F125W	23.13	0.04
F160W	23.34	0.07

[a]Values in this table have not been corrected for Galactic extinction.

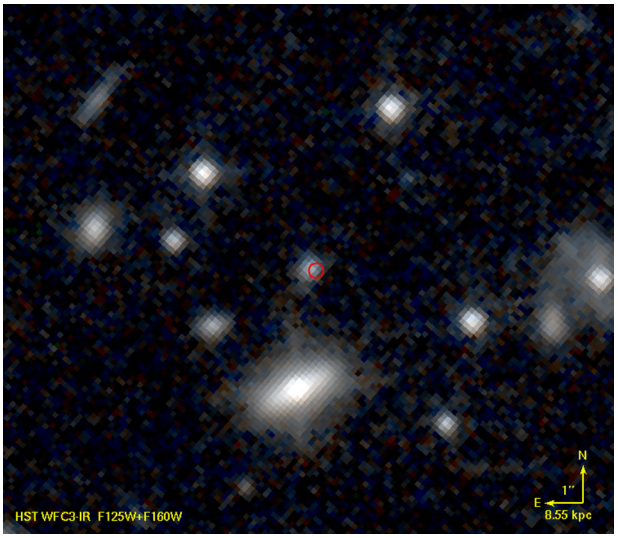

Figure 9. False-colour NIR *HST* imaging of the field of GRB 120119A using the *F125W* and *F160W* filters of WFC3-IR, taken 9 months after the GRB. The host galaxy appears as a compact source centred slightly east of the optical position (red circle) with some extension in the north-west and south–south-east directions. Given the redshift of the host, the blue colour suggests substantial line contribution to the *J* band and a very large specific star formation rate. There are no obvious signs of ongoing interaction at this resolution. The limiting magnitudes of the image are $F125W = 25.6$ and $F160W = 25.4$ (AB).

at 1–7 d) indicates that contribution of an afterglow to our photometry of the host galaxy at 4 d and later is essentially negligible, allowing us to categorize the properties of the host photometrically. Our host photometry is given in Table 6 and our *HST* imaging is shown in Fig. 9. The host colour is observed to be quite red (although not quite as red as the afterglow), with $R - K = 3.6$ mag (2.0 mag AB) after correction for Galactic reddening. This value is much redder than typical unobscured GRB hosts (Le Floc'h et al. 2003; Hjorth et al. 2012) and fairly characteristic of the 'dark' GRB host population (Krühler et al. 2011; Rossi et al. 2012; Perley et al. 2013).

We fit the combined data set to a range of simple population-synthesis models with Calzetti et al. (2000) extinction and constant star formation history. Importantly, our models include an empirical treatment of nebular emission lines based on the relations of Kennicutt (1998), Kewley & Dopita (2002), and Kewley, Geller & Jansen (2004).

The resulting SED is nearly flat in νF_ν with no evidence of a Balmer break, indicating a young population. A large upturn is evident in the *F125W* filter relative to all other bands; this feature is highly significant (given the excellent quality of the *HST* photometry) and cannot be explained by any model invoking the stellar continuum alone. This feature probably results from the [O III] and Hβ emission lines falling within the *F125W* bandpass – which, given the strength of the upturn, would imply that these features contribute approximately a third of the flux in the *F125W* broad-band filter. This implies an extremely young stellar population. Based on our SED fitting procedure, we estimate a current star formation rate of $\sim 200\,M_\odot\,\mathrm{yr}^{-1}$ and a stellar mass of only $M \approx 2 \times 10^9\,M_\odot$. The mean attenuation is $A_V \approx 1.8$ mag, indicating a quite dusty galaxy.

These properties suggest a young, vigorously star-forming, dusty galaxy, with a star formation rate 100 times larger than that of the MW despite a mass comparable to that of the LMC. Given the extreme inferred star formation rate, we predict that the nebular lines of this host should be easily detectable with NIR spectroscopy, and the host should be detectable with current radio and millimetre/submillimetre facilities as well. The small size of the galaxy and the concentration of most of the light in the core indicate that much of this star formation is occurring within a very small volume ($\lesssim$1 arcsec in diameter, corresponding to 8 kpc) and over a very short time-scale ($\sim 10^7$ yr) without an obvious merger trigger apparent in our imaging, although it is possible that even higher resolution observations [with *HST* Wide Field Camera 3 (WFC3)-Ultraviolet Imaging Spectrograph (UVIS) or Advanced Camera for Surveys (ACS), or Atacama Large Millimeter/submillimeter Array (ALMA)] will resolve the core into a late-stage merger.

4 DISCUSSION AND CONCLUSIONS

The photodestruction of dust in the environments of GRBs is expected to occur at early times after the initial blast of high-energy radiation (Perna & Loeb 1998; Waxman & Draine 2000; Draine & Hao 2002). Simultaneous, multicolour imaging of the afterglow (especially during the high-intensity, high-energy emission) is necessary to observe both the decrease in opacity and red-to-blue colour change associated with dust destruction (Fruchter et al. 2001; Perna et al. 2003). Perley et al. (2010) tested for this in the case of GRB 071025 with simultaneous $J\,H\,K_s$ and unfiltered optical data (which resembled the *I* band due to the redness of the afterglow). They binned the optical and NIR measurements to temporally match, and dust models were fit at each four-point SED, allowing both the extinction and intrinsic spectral index β to vary. No evidence for a change in absorption was seen, notably during the first bin, which coincides with the end of the prompt X-ray emission, ruling out dust destruction after the start of the NIR observations ($\sim$150 s).

We extended upon this methodology for GRB 120119A by performing interpolation via natural cubic regression splines to the densely sampled PAIRITEL data, which could then be combined with our other photometry (most notably the usually simultaneous PROMPT *R* and *I* filters) to create a dense temporal series of early-time SEDs (Section 3.3). The extinction properties inferred from late-time data were held as fixed (Fig. 4), and β was fit to each SED. We then explored whether allowing the extinction to vary with time could improve the fit (Fig. 4).

Both A_V and R_V (the latter of which we left fixed in our modelling) are expected to change with time in non-trivial ways under the influence of a high-intensity, high-energy radiation field. Detailed dust-destruction simulations by Perna et al. (2003) present the time evolution of extinction and reddening for a variety of environments (density and radius), dust distributions, and dust-to-gas ratios. These

simulations highlight the complex interplay between changes in extinction and reddening with time and are highly dependent on the local environment. Note also that these simulations assume a constant luminosity from the X-ray source, and a fixed spectral index ($\beta = 0.5$). A changing luminosity of the photoionizing radiation and a changing spectral index, as are present in GRB prompt emission, further complicate the issue. Choosing a rigorous parametric model to fit (and inferring meaningful constraints on its parameters) would be very difficult without detailed simulations allowing for the effects of changing luminosities and spectral indices.

Regardless, our relatively simplistic choice of functional forms for how $A_V(t)$ and $\beta(t)$ could vary (equations 3 and 4) did in fact cause a statistically significant improvement in the overall fit compared to a fixed A_V. While not definitively implying dust destruction in GRB 120119A, simultaneous changes in A_V and β can account for the variations in the SED much better than a changing β alone.

Within the assumptions of the model, and by fixing the late-time extinction parameters to the best-fitting values derived in Section 3.2, the extinction A_V is expected to decrease by an average of 0.61 ± 0.15 mag (Fig. 7), with at least $\sim$0.15 mag of extinction change to a 99.73 per cent level (3σ; Fig. 8). Alternative parametric models may be more appropriate, but the limited spectral coverage at each temporal point prevents stringent model selection. Moreover, the inference of dust destruction appears to be robust against the exact choice of assumed late-time extinction curve, as all reasonable tested dust models resulted in this conclusion (after fixing the late-time A_V and β to their best-fitting values for each particular model). In further support of the general conclusion of dust destruction, we note that the bulk of the colour change is ongoing during the tail end of the high-intensity X-ray emission, during which dust destruction is expected to occur (Fruchter et al. 2001).

Finally, we note that this work highlights the importance of well-sampled, multicolour early-time observations afforded by small and nimble fully robotic telescopes quickly training on the GRB location. Delays of seconds matter at this stage of the evolution of the GRB, and the importance of observation speed outweighs that of observation depth. The combination of shallow-and-fast robotic follow-up observations with deep late-time observations across the electromagnetic spectrum is necessary to illustrate the full story behind the evolution of GRB afterglows, which still to this day are revealing new insights.

ACKNOWLEDGEMENTS

PAIRITEL is operated by the Smithsonian Astrophysical Observatory (SAO) and was made possible by a grant from the Harvard University Milton Fund, a camera loan from the University of Virginia, and continued support of the SAO and UC Berkeley. The PAIRITEL project is further supported by NASA/*Swift* Guest Investigator grants NNX10AI21G and NNX12AD73G. We utilized observations obtained at the Gemini Observatory, which is operated by the Association of Universities for Research in Astronomy, Inc., under a cooperative agreement with the NSF on behalf of the Gemini partnership: the NSF (USA), the Science and Technology Facilities Council (UK), the National Research Council (Canada), CONICYT (Chile), the Australian Research Council (Australia), Ministèrio da Ciência, Tecnologia e Inovação (Brazil), and Ministerio de Ciencia, Tecnología e Innovación Productiva (Argentina). The Liverpool Telescope is operated on the island of La Palma by Liverpool John Moores University in the Spanish Observatorio del Roque de los Muchachos of the Instituto de Astrofisica de Canarias with financial support from the UK Science and Technology Facilities Council. KAIT and its ongoing operation were made possible by donations from Sun Microsystems, Inc., the Hewlett-Packard Company, AutoScope Corporation, Lick Observatory, the NSF, the University of California, the Sylvia and Jim Katzman Foundation, and the TABASGO Foundation. Some of the data presented herein were obtained at the W. M. Keck Observatory, which is operated as a scientific partnership among the California Institute of Technology, the University of California, and NASA; the Observatory was made possible by the generous financial support of the W. M. Keck Foundation. We wish to extend special thanks to those of Hawaiian ancestry on whose sacred mountain we are privileged to be guests. We are grateful to the staffs at the Gemini, Keck, and Lick Observatories for their assistance. This publication has made use of data obtained from the *Swift* interface of the High-Energy Astrophysics Archive (HEASARC), provided by NASA's Goddard Space Flight Center. We sincerely thank the *Swift* team for the rapid public dissemination, calibration, and analysis of the *Swift* data. We also thank Scott Barthelmy for his invaluable efforts in creating and maintaining the GCN system.

We thank the anonymous referee for useful comments on this paper. We also thank Alex Kann for providing helpful suggestions to the text. CGM acknowledges support from the Royal Society. AVF's group at UC Berkeley has received generous financial assistance from Gary and Cynthia Bengier, the Christopher R. Redlich Fund, the Richard and Rhoda Goldman Fund, the TABASGO Foundation, NSF grant AST-1211916, and NASA/*Swift* grants NNX10AI21G and NNX12AD73G. AG acknowledges funding from the Slovenian Research Agency and from the Centre of Excellence for Space Science and Technologies SPACE-SI, an operation partly financed by the European Union, the European Regional Development Fund, and the Republic of Slovenia. Support for this work was provided by NASA to DAP through Hubble Fellowship grant HST-HF-51296.01-A awarded by the Space Telescope Science Institute, which is operated for NASA by AURA, Inc., under contract NAS 5-26555. We dedicate this paper to the memory of Weidong Li, who developed the software for KAIT automatic follow-up observations of GRBs; we deeply miss his friendship and collaboration, which were tragically taken away from us much too early.

REFERENCES

Aihara H. et al., 2011, ApJS, 193, 29
Barthelmy S. D. et al., 2005, Space Sci. Rev., 120, 143
Bertin E., Arnouts S., 1996, A&AS, 117, 393
Bertin E., Mellier Y., Radovich M., Missonnier G., Didelon P., Morin B., 2002, in Bohlender D. A., Durand D., Handley T. H., eds, ASP Conf. Ser. Vol. 281, Astronomical Data Analysis Software and Systems XI. Astron. Soc. Pac., San Francisco, p. 228
Beuermann K. et al., 1999, A&A, 352, L26
Bloom J. S., Kulkarni S. R., Djorgovski S. G., 2002, AJ, 123, 1111
Bloom J. S., Starr D. L., Blake C. H., Skrutskie M. F., Falco E. E., 2006, in Gabriel C., Arviset C., Ponz D., Enrique S., eds, ASP Conf. Ser. Vol. 351, Astronomical Data Analysis Software and Systems XV. Astron. Soc. Pac., San Francisco, p. 751
Bloom J. S. et al., 2009, ApJ, 691, 723
Burrows D. N. et al., 2005, Space Sci. Rev., 120, 165
Butler N. R., Kocevski D., 2007, ApJ, 663, 407
Butler N. R., Kocevski D., Bloom J. S., Curtis J. L., 2007, ApJ, 671, 656
Calzetti D., Armus L., Bohlin R. C., Kinney A. L., Koornneef J., Storchi-Bergmann T., 2000, ApJ, 533, 682
Cenko S. B. et al., 2006, PASP, 118, 1396
Cenko S. B. et al., 2009, ApJ, 693, 1484
Chester M. M., Beardmore A. P., 2012, GRB Coordinates Network, 12880, 1

Covino S. et al., 2013, MNRAS, 432, 1231
Cucchiara A., Jones T., Charlton J. C., Fox D. B., Einsig D., Narayanan A., 2009, ApJ, 697, 345
Draine B. T., Hao L., 2002, ApJ, 569, 780
Elíasdóttir Á. et al., 2009, ApJ, 697, 1725
Filippenko A. V., Li W. D., Treffers R. R., Modjaz M., 2001, in Paczynski B., Chen W.-P., Lemme C., eds, ASP Conf. Ser. Vol. 246, IAU Colloq. 183, Small Telescope Astronomy on Global Scales. Astron. Soc. Pac., San Francisco, p. 121
Fitzpatrick E. L., 1999, PASP, 111, 63
Fruchter A., Krolik J. H., Rhoads J. E., 2001, ApJ, 563, 597
Galama T. J. et al., 1999, Nature, 398, 394
Gehrels N. et al., 2004, ApJ, 611, 1005
Golenetskii S. et al., 2012, GRB Coordinates Network, 12872, 1
Gomboc A. et al., 2008, ApJ, 687, 443
Gordon K. D., Clayton G. C., Misselt K. A., Landolt A. U., Wolff M. J., 2003, ApJ, 594, 279
Granot J., Sari R., 2002, ApJ, 568, 820
Gruber D., 2012, GRB Coordinates Network, 12874, 1
Guidorzi C. et al., 2006, PASP, 118, 288
Guidorzi C. et al., 2011, MNRAS, 417, 2124
Hjorth J. et al., 2012, ApJ, 756, 187
Hodapp K. W. et al., 2003, PASP, 115, 1388
Hook I. M., Jørgensen I., Allington-Smith J. R., Davies R. L., Metcalfe N., Murowinski R. G., Crampton D., 2004, PASP, 116, 425
Jester S. et al., 2005, AJ, 130, 873
Kalberla P. M. W., Burton W. B., Hartmann D., Arnal E. M., Bajaja E., Morras R., Pöppel W. G. L., 2005, A&A, 440, 775
Kann D. A. et al., 2010, ApJ, 720, 1513
Kann D. A. et al., 2011, ApJ, 734, 96
Kennicutt R. C., Jr, 1998, ARA&A, 36, 189
Kewley L. J., Dopita M. A., 2002, ApJS, 142, 35
Kewley L. J., Geller M. J., Jansen R. A., 2004, AJ, 127, 2002
Krühler T. et al., 2008, ApJ, 685, 376
Krühler T. et al., 2011, A&A, 534, A108
Kulkarni S. R. et al., 1999, ApJ, 522, L97
Landolt A. U., 1992, AJ, 104, 340
Le Floc'h E. et al., 2003, A&A, 400, 499
Li W., Filippenko A. V., Chornock R., Jha S., 2003a, ApJ, 586, L9
Li W., Filippenko A. V., Chornock R., Jha S., 2003b, PASP, 115, 844
Liang E.-W., Racusin J. L., Zhang B., Zhang B.-B., Burrows D. N., 2008, ApJ, 675, 528
Melandri A. et al., 2008, ApJ, 686, 1209
Melandri A. et al., 2010, ApJ, 723, 1331
Mészáros P., 2006, Rep. Progress Phys., 69, 2259
Misselt K. A., Clayton G. C., Gordon K. D., 1999, ApJ, 515, 128
Oates S. R. et al., 2009, MNRAS, 395, 490
O'Brien P. T. et al., 2006, ApJ, 647, 1213
Oke J. B. et al., 1995, PASP, 107, 375
Panaitescu A., Vestrand W. T., 2008, MNRAS, 387, 497
Perley D. A. et al., 2008a, ApJ, 672, 449
Perley D. A. et al., 2008b, ApJ, 688, 470
Perley D. A. et al., 2010, MNRAS, 406, 2473
Perley D. A. et al., 2011, AJ, 141, 36
Perley D. A. et al., 2013, ApJ, 778, 128
Perley D. A. et al., 2014, ApJ, 781, 37
Perna R., Loeb A., 1998, ApJ, 501, 467
Perna R., Lazzati D., Fiore F., 2003, ApJ, 585, 775
Piran T., 2005, Rev. Modern Phys., 76, 1143
Prochter G. E., Prochaska J. X., Burles S. M., 2006, ApJ, 639, 766
Racusin J. L. et al., 2008, Nature, 455, 183
Richards J. W., Homrighausen D., Freeman P. E., Schafer C. M., Poznanski D., 2012, MNRAS, 419, 1121
Roming P. W. A. et al., 2005, Space Sci. Rev., 120, 95
Rossi A. et al., 2012, A&A, 545, A77
Ruppert D., Wand M., Carroll R., 2003, Semiparametric Regression. Cambridge Univ. Press, Cambridge
Rykoff E. S. et al., 2004, ApJ, 601, 1013
Rykoff E. S. et al., 2009, ApJ, 702, 489
Sari R., Piran T., Narayan R., 1998, ApJ, 497, L17
Schady P. et al., 2010, MNRAS, 401, 2773
Schady P. et al., 2012, A&A, 537, A15
Schlafly E. F., Finkbeiner D. P., 2011, ApJ, 737, 103
Schlegel D. J., Finkbeiner D. P., Davis M., 1998, ApJ, 500, 525
Skrutskie M. F. et al., 2006, AJ, 131, 1163
van Dokkum P. G., 2001, PASP, 113, 1420
Vergani S. D., Petitjean P., Ledoux C., Vreeswijk P., Smette A., Meurs E. J. A., 2009, A&A, 503, 771
Wasserman L., 2006, All of Nonparametric Statistics. Springer-Verlag, Berlin
Watson D., Jakobsson P., 2012, ApJ, 754, 89
Waxman E., Draine B. T., 2000, ApJ, 537, 796
Yost S. A., Harrison F. A., Sari R., Frail D. A., 2003, ApJ, 597, 459
Zafar T. et al., 2012, ApJ, 753, 82
Zauderer A., Berger E., 2012, GRB Coordinates Network, 12895, 1

SUPPORTING INFORMATION

Additional Supporting Information may be found in the online version of this article:

Table 1. Photometry of GRB 120119A (http://mnras.oxfordjournals.org/lookup/suppl/doi:10.1093/mnras/stu344/-/DC1).

Please note: Oxford University Press is not responsible for the content or functionality of any supporting materials supplied by the authors. Any queries (other than missing material) should be directed to the corresponding author for the article.

This paper has been typeset from a TEX/LATEX file prepared by the author.